A novel CoP@AAH cocatalyst leads to excellent stability and enhanced photocatalytic H$_2$ evolution of CdS by structurally separating the photogenerated carriers

Junnan Tao [a],[1], Mingyuan Wang [b],[1], Xiangzhao Zhang [a], Lei Lu [a], Hua Tang [c],[*], Qinqin Liu [a], Shuangying Lei [b], Guanjun Qiao [a], Guiwu Liu [a],[*]

[a] *School of Materials Science and Engineering, Jiangsu University, Zhenjiang, Jiangsu 212013, China*
[b] *SEU-FEI Nano-Pico Center, Key Laboratory of MEMS of Ministry of Education, School of Electrical Science and Engineering, Southeast University, Nanjing 210096, China*
[c] *School of Environmental Science and Engineering, Qingdao University, Qingdao 266071, China*

ABSTRACT

To alleviate the fast recombination of charges and enhance the stability of CdS, a novel CoP@amorphous aluminum hydroxide (AAH) cocatalyst was developed and loaded on CdS nanorods via an in-situ phosphorization process to structurally separate the photogenerated carriers. The AAH completely covers the CdS nanorods to form a core-shell structure, and the high-conductivity CoP nanoparticles embedded in the AAH shell act as a charge transfer bridge, making the H$_2$ evolution reaction sites migrate far from CdS and thus prevent the photocorrosion derived from the accumulation of photogenerated holes. The optimized CdS/CoP@AAH hybrid catalyst presents a photocatalytic H$_2$ evolution rate of 54.9 mmol/g/h, apparent quantum efficiency of 40.62% and excellent cycle stability. DFT calculations were also employed from the views of band structure and Gibbs free energy to illuminate the photocatalytic mechanism. This work offers a new strategy to restrain the photocorrosion and enhance the photocatalytic H$_2$ production of CdS-based catalysts simultaneously.

1. Introduction

Being constrained by the shortage of energy, people are urgently looking for a clean and renewable energy to replace the traditional fossil fuels [1–3]. As a potential new energy source, hydrogen energy derived from photocatalysis attracts many attentions [4–7]. CdS is regarded as a promising catalyst due to its suitable band gap width, negative conduction potential and good visible light absorption capacity [8–12]. However, the lack of surface-active sites and the high recombination rate of photogenerated carriers bring about a relatively low light utilization [13–16]. In particular, the photocorrosion in CdS-based catalysts derived from the accumulation of photogenerated holes can seriously restrict their practical applications [17–21]. So, the key to solving this problem is to improve the charge separation, thus alleviating the oxidation of S^{2-} and the reduction of Cd^{2+}.

A commonly used method is to combine a cocatalyst with CdS in order to enhance the separation of photogenerated carries, and meanwhile the cocatalyst with high-conductivity can avert the accumulation of photogenerated carriers [22,23]. Traditional noble metals (such as Pt, Pd and Au) used to undertake this role, but their high prices and scarcity compel people to look for a substitution [24,25]. Furthermore, simply loading noble metal nanoparticles on the CdS surface cannot structurally separate the photogenerated carriers [26–28]. Accordingly, numerous investigations focus on non-noble metal cocatalysts. For instance, Li et al. designed a 2D/2D CdS/P-doped NiS heterojunction, and confirmed that the P-doped NiS can improve water reduction kinetics and boost the separation of photo-induced carries to enhance the photocatalytic H$_2$ evolution reaction (HER) and stability [29]. Lu et al. constructed a NiP/CdS core-shell structure, which enables the photogenerated carries to transfer out of the shell and thus alleviates the oxygen leading CdS photocorrosion with the assistance of artificial gill [30]. Xu et al. prepared a 2D/2D CdS/Ti$_3$C$_2$ composite, and demonstrated that the Ti$_3$C$_2$ nanosheets can contribute to in-situ confining the leaching of Cd^{2+} ions, thus preventing the

---

decomposition of CdS caused by photocorrosion [31]. Although the high photocatalytic H$_2$ production rates coupled with good anti-photocorrosion were claimed in these works, the charge separation is somewhat inefficient since the photogenerated carriers are not far from the semiconductor catalyst. Hence, a new strategy should be proposed to structurally separate the photoinduced carriers from CdS.

Transition metal phosphides (TMPs) are usually adopted to be co-catalysts due to the high electronic conductivity, good chemical stability and relatively low HER overpotentials [32,33]. However, a direct loading of TMP usually cannot meet the requirement of high spatial separation in photocatalytic system, so the single cocatalyst needs to be modified to get composite systems. Indeed, transition metal hydroxides (TMHs) are always used as the precursors during the preparation of TMPs [34,35]. In particular, a binary hybrid cocatalyst can be acquired after the phosphorization of layered double hydroxides (LDHs), with a general formula of M$_{1-x}^{2+}$M$_x^{3+}$(OH)$_2$, where M^{2+} and M^{3+} denote divalent and trivalent cations [36–38].

Inspired by this, a novel CoP@AAH binary cocatalyst was designed to cover on CdS nanorods by an in-situ phosphorization method using CoAl-LDH hybrid as precursor. The CdS/CoP@AAH ternary hybrid possesses a well-defined core-shell structure, and especially the highly conductive CoP nanoparticles embedded in the AAH shell can act as a bridge for charge transfer, which can make the HER far from CdS and thus effectively enhance the anti-photocorrosion and H$_2$ evolution performance of CdS. The optimized CdS/CoP@AAH hybrid catalyst presents the photocatalytic H$_2$ evolution rate of 54.9 mmol/g/h (~15 times higher than that of pristine CdS), apparent quantum efficiency (AQE) of 40.62% and excellent cycle stability. Moreover, the photocatalytic H$_2$ production mechanism is proposed by combining the experiments and first-principles calculations.

2. Experimental and calculation procedures

2.1. Synthesis of CdS nanorods, CdS/CoAl-LDH, CdS/CoP@AAH hybrids

Cd(NO$_3$)$_2$·4H$_2$O (4.62 g) and CH$_4$N$_2$S (3.43 g) were dissolved in ethanediamine (40 mL) and stirred for 1 h, and then the resulting solution was transferred into a 50 mL Teflon-lined autoclave, sealed and maintained at 160 °C for 48 h. After cooling down, the precipitates were washed with deionized (DI) water and ethanol repeatedly, then dried in 70 °C for 12 h to get CdS nanorods.

A certain quantity of CdS nanorods (150, 250, 350, 500 or 650 mg) was dispersed into 80 mL DI water and sonicated for 1 h, and then Co(NO$_3$)$_2$·6H$_2$O (0.546 g) and Al$_2$(NO$_3$)$_3$·9H$_2$O (0.235 g) was added into the suspension and stirred for 6 h, which can make the Co^{2+} and Al^{3+} anchor tightly on the CdS nanorods with negative charge (−15.4 mV, Fig. S1). Subsequently, CH$_4$N$_2$O (0.35 g) and NH$_4$F (0.0925 g) were added into the mixed suspension and stirred for 2 h, then transferred into a 100 mL Teflon-lined autoclave, sealed and maintained at 120 °C for 10 h. After cooling down, the precipitates were washed with DI water and ethanol repeatedly, then dried in 70 °C for 12 h. The as-obtained
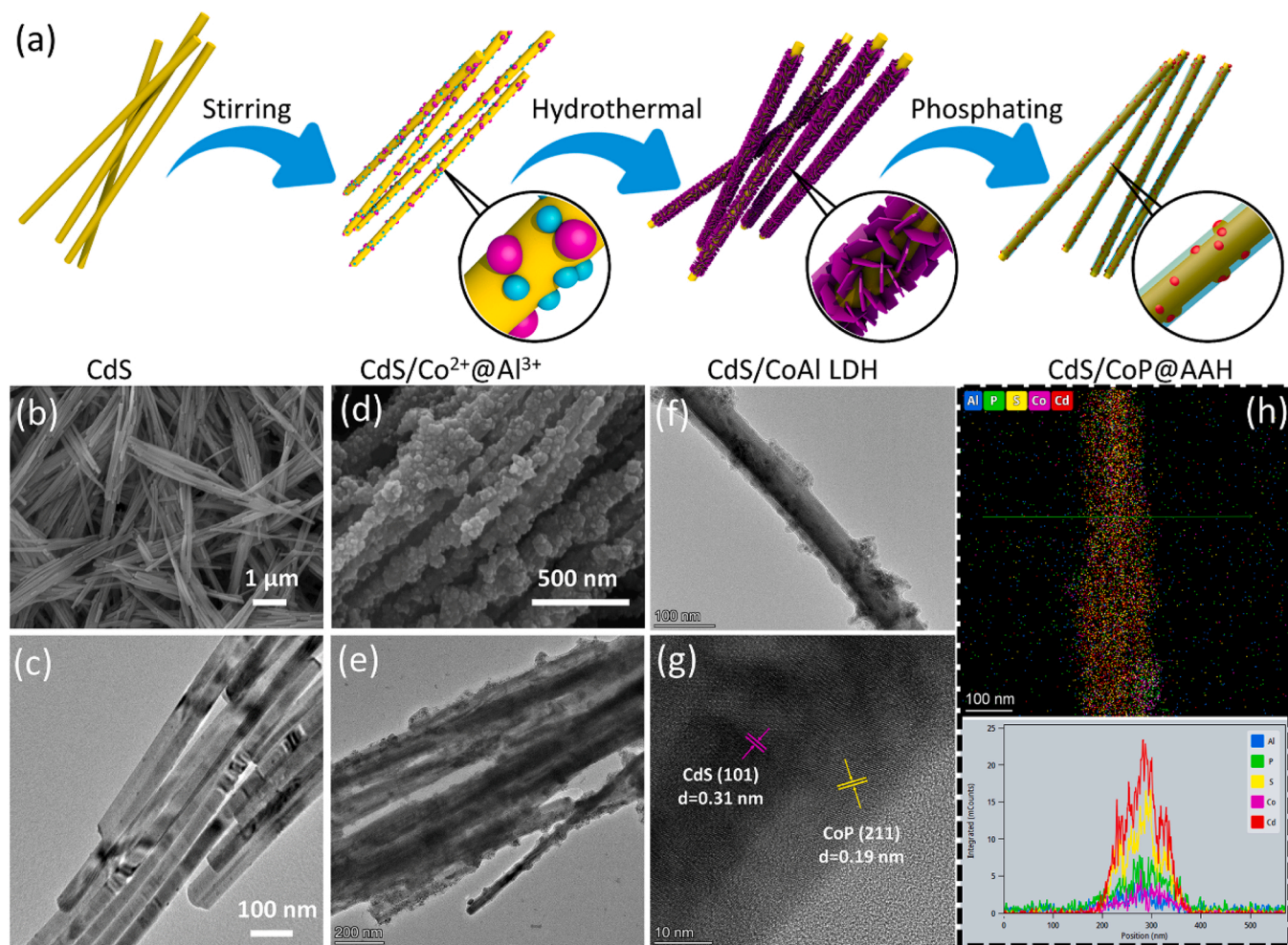

Fig. 1. (a) Schematic of synthesis of CdS/CoP@AAH hybrids; SEM, TEM and HRTEM images of (b,c) CdS and (d—g) CLP-350 hybrid; (h) Elemental EDS profiles of a CdS nanorod covered by CoP@AAH cocatalyst in the CLP-350 hybrid.

CdS/CoAl-LDH hybrid samples are denoted as CL-150, CL-250, CL-350, CL-500 and CL-650, respectively.

Typically, for an in-situ phosphorization method, 50 mg of the above-mentioned CdS/CoAl-LDH hybrids and 500 mg of $NaH_2PO_2 \cdot H_2O$ were added into 20 mL ethanol, stirred for 7 h and evaporated to dryness, then transferred into ceramic crucible and maintained at 300 °C for 2 h in Ar atmosphere. After cooling down, the resulting powders were washed centrifugally with DI water and ethanol repeatedly, then dried in 70 °C for 12 h. The as-prepared (CdS/CoP@AAH) hybrid samples are denoted as CLP-150, CLP-250, CLP-350, CLP-500 and CLP-650, respectively. Fig. 1a shows the schematic of synthesis of CdS/CoP@AAH hybrids.

For comparison, the corresponding samples derived from 350 mg CdS nanorods, 0.546 g $Al_2(NO_3)_3 \cdot 9H_2O$ or 0.235 g $Co(NO_3)_2 \cdot 6H_2O$ and 500 mg of $NaH_2PO_2 \cdot H_2O$ were also prepared, which are denoted as CAP-350 and CCP-350, respectively. The ex-situ phosphorization method was also employed. Typically, 50 mg of the CL-350 hybrid or LDH and 500 mg of $NaH_2PO_2 \cdot H_2O$ were placed on the two sides of a porcelain boat, respectively, and maintained at 300 °C for 2 h in Ar atmosphere. The as-fabricated corresponding samples are denoted as CLP-350-ex and LDH-P-ex, respectively. The Pt loaded CdS was prepared via a light deposition process. Typically, 50 mg CdS nanorods was ultrasonically dispersed in 80 mL water in a 100 mL three-necked flask. Then 400 μL H_2PtCl_6 (10 mg/mL) was added into the suspension. The suspension was placed under light irradiation (300 W Xe light). After stirring for 2 h, the suspension was washed with deionized water and ethanol repeatedly, then dried in 70 °C for 12 h. The as-obtained sample is denoted as CdS/Pt.

2.2. Microstructural and microchemical characterizations

X-ray diffractometer (XRD, D/MAX2500PC) was used to determine the crystal structures and phase compositions. Field emission scanning electron microscopy (FE-SEM, FEI Nova Nano 450) and transmission electron microscope (TEM, FEI Tecnai G2F30 S-TWIN) equipped with energy dispersive spectrometer (EDS) were employed to observe and analyze the morphology and interfacial structure. X-ray photoelectron spectroscopy (XPS) analysis was carried out on a PHI ESCA5000C electron spectrometer to determine the binding states of elements. The absorption spectra were recorded on a UV-2450 spectrophotometer (Shimadzu, Japan) using $BaSO_4$ as a reference in the range of 200–1400 nm. The photoluminescence (PL) and time resolution photoluminescence (TRPL) spectroscopy spectra were recorded by exploiting fluorescence spectrophotometer (Hitachi, F-7000) with a laser light resource using the excitation wavelength of 360 nm. The electron spin resonance (ESR) spectra were acquired on Bruker A300–10/12 spectrometer using 2, 2, 6, 6-tetramethyl-piperidine-1-oxyl (TEMPO) as radical scavenger. The concentration of Cd^{2+} was measured by inductively coupled plasma-optical emission spectrometry (ICP-OES) on an atomic absorption spectrometer (AA300, AAS CONTR).

2.3. Photoelectrochemical measurement

An electrochemical workstation (Chenhua Instruments, CHI660D) was employed to measure the photocurrent response, electrochemical impedance spectroscopy (EIS), cyclic voltammetry (CV), linear sweep voltammetry (LSV) and Mott–Schottky (M-S) plots. The three-electrode system consists of the Ag/AgCl reference electrode, Pt foil counter electrode and working electrode, where 1 M KOH solution was used as electrolyte. The bias voltage was set as 0.6 V. The working electrode was prepared as follows: 10 mg of sample was added into a mixed solution (involving 500 μL ethanol, 500 μL ethylene glycol and 80 μL Nafion solution), then dispersed ultrasonically to obtain a homogeneous suspension, and finally 80 μL suspension was coated on fluorine-doped tin oxide (FTO) glass and dried in 70 °C for 12 h. The surface photovoltage (SPV) plots were recorded on a CEL-SPS1000 instrument.

2.4. Photocatalytic H_2 production

The photocatalytic H_2 evolution of as-prepared samples was measured under a 300 W Xe lamp with a UV-cutoff filter ($\lambda > 400$ nm). For a typical H_2 production reaction, 10 mg of sample and 80 mL 10 vol % lactic acid (or 80 mL deionized water) were added in a 100 mL three-neck flask, then ultrasonically treated for 5 min to get a homogeneous suspension. The photocatalytic H_2 evolution was measured by an online gas chromatograph (Shimadzu, GC-8A) coupled with a thermal conductivity detector, and N_2 was used as the carrier gas. The apparent quantum efficiency (AQE) was calculated for different incident monochromatic wavelengths (420, 450,550 and 650 nm) according to the following equation:

$$AQE = \frac{2 \times \text{number of } H_2 \text{ molecules (n)}}{\text{Number of incident photos (N)}} \quad (1)$$

2.5. Gibbs free energy and band structure calculations

The first-principles calculations were performed by the Vienna Ab-initio Simulation Package (VASP) code based on density functional theory (DFT). The generalized gradient approximation (GGA) in the Perdew-Burke-Ernzerhof (PBE) form was used for the exchange correlation [39,40]. The typical facet of CdS was adopted as its surface and described by a 4×3 supercell with three Cd-S layers. The plane-wave cut-off energy and convergence criterion were set as 400 and 10^{-4} eV, respectively. A convergence threshold was set 0.01 eV/Å in force. To calculate the total energy of defect, a $3 \times 3 \times 1$ primitive cell was used for modeling the intrinsic and extrinsic defects, and the Γ point calculations were employed. The interfaces between H and CdS, CoP@CdS, $Al_2(OH)_3F_2$ were investigated. The Gibbs free energy ΔG_{H*} was calculated to evaluate the computational high-throughput screening of photocatalytic materials for H_2 evolution:

$$\Delta G_{H*} = \Delta E_H + \Delta E_{ZPE} - T\Delta S_H \quad (2)$$

where ΔE_H represents the hydrogen adsorption energy, which is defined as:

$$\Delta E_H = E_{(catalyst-H*)} - E_{(catalyst)} - \frac{1}{2}E_H \quad (3)$$

where $E_{(catslyst-H*)}$, $E_{(catalyst)}$ and E_H are the energies for the H* adsorption on catalyst surface, catalyst and hydrogen, respectively; ΔE_{EZP} represents the change in zero-point energy, which is calculated by the vibration frequency:

$$\Delta E_{ZPE} = \frac{1}{2}\sum_i h\nu i \quad (4)$$

where h and ν are Planck constant and vibrational frequency; T is the absolute temperature (298.15 K), and ΔS_H denotes the change of entropy, which is defined by:

$$\Delta S_H = -1/2S_{H2}^0 \quad (5)$$

where S_{H2}^0 is the entropy of H_2 in gas phase under the standard conditions.

3. Results and discussion

3.1. Synthesis and characterization of different samples

As shown in Fig. S2a, the diffraction peaks for CdS nanorods are assigned to the well-crystallized CdS (JCPDS. 41–1049) in the CdS/CoAl-LDH hybrids, and meanwhile the LDH is in accordance with the lattice diffraction of typical LDH (JCPDS. 48–1022, Fig. S2c), indicating a good combination between the CdS and CoAl-LDH. Apparently, the

characteristic peaks of CoAl-LDH strengthen gradually with the addition amount of CdS decreasing. However, no other diffraction peaks appear except those of CdS when the CdS/CoAl-LDH hybrids were treated by in-situ phosphorization method (Fig. S2b). Actually, the peaks of orthorhombic CoP (JCPDS. 29–0497) can be detected after in-situ phosphorization of CoAl-LDH (Fig. S2d). Furthermore, the XRD results confirm the formation of $Al_2(OH)_3F_2$ and the absence of CoP while employing the ex-situ phosphorization process (Fig. S2e), and the centrifugal washing in the in-situ phosphorization process doesn't need to be responsible for the disappearance of $Al_2(OH)_3F_2$ (Fig. S2f). All these results indicate that the in-situ phosphorization process can destroy the crystallinity of $Al_2(OH)_3F_2$, resulting in formation of CoP and amorphous AAH. Indeed, well-developed nanorods are formed in the pristine CdS, with smooth surface and a width of ~40 nm (Fig. 1b and c). Flower-like microspheres of ~Ø6 μm, consisting of nanosheets, are produced in the pristine CoAl-LDH (Fig. S3a). However, the CoAl-LDH nanosheets (rather than microspheres) cover uniformly and densely on the CdS nanorods after adding the CdS nanorods, forming a 3D nanosheets network structure (Fig. S3b). After in-situ phosphorization, these CoAl-LDH nanosheets disappear (Fig. S3c), and meanwhile the smooth surface of CdS nanorods turns into rough one, which can be attributed to the complete coverage of AAH on the CdS nanorods and the embedment of CoP particles in the AAH coating, producing a unique core-shell structure (Fig. 1d—f). The corresponding EDS elemental mapping further demonstrates the complete and uneven coverage (Fig. 1h and S4). Actually, this coverage leads to good linking between CdS nanorods, demonstrated by the decrease of surface area and pore volume (Fig. S5a and b), which can provide unobstructed charge transfer pathway. For comparison, the flower-like structure is retained after the ex-situ phosphorization of CoAl-LDH (Fig. S3d), and the smooth CdS nanorods still appear in CLP-350-ex hybrid (Fig. S3e), indicating that the unique core-shell structure cannot be produced while employing the ex-situ phosphorization process. Moreover, only CoP nanoparticles are attached on the CdS nanorods due to no addition of $Al_2(NO_3)_3 \cdot 9H_2O$ (Fig. S3f), while only the big octahedral $Al_2(OH)_3F_2$ grains scatter in the CdS nanorods

owing to no introduction of $Co(NO_3)_2 \cdot 6H_2O$ (Fig. S3g and h), implying that the formation of AAH coating on the CdS nanorods depends totally on the additions of both $Al_2(NO_3)_3 \cdot 9H_2O$ and $Co(NO_3)_2 \cdot 6H_2O$ via the in-situ phosphorization process. Moreover, the HR-TEM image of CdS/CoP@AAH interface demonstrates that the lattice fringe spacings of 0.19 and 0.31 nm correspond to the (211) and (101) planes of CoP and CdS, respectively, indicating a direct contact between CoP and CdS (Fig. 1g). Therefore, the imbedding of CoP into the AAH, complete coverage and direct contact can contribute to the outward transport of the photo-generated carriers from the core to shell, which can contribute to enhancing the charge separation and avoiding photocorrosion.

As expected, the peaks of Cd and S of CdS/CoP@AAH hybrid sharply drop compared with those of the pristine CdS (Fig. 2a), accompanying with the appearance of the P 2p and Co 2p peaks. For the Cd 3 spectra, the two peaks at ~405 and 411 eV can be assigned to the Cd $3d_{5/2}$ and Cd $3d_{3/2}$, respectively, and the two peaks for CLP-350 shift towards higher binding energy (Fig. 2b), which is mainly derived from the charge transfer from CdS to CoP at the interface [41–43]. Similarly, the two S peaks located at ~161 and 163 eV, corresponding to the S $2p_{3/2}$ and S $2p_{1/2}$, also shift towards higher binding energy (Fig. 2c). Moreover, the two main peaks at 781.8 and 797.8 eV are assigned to Co $2p_{3/2}$ and Co $2p_{1/2}$, and they are surrounded by two pairs of satellite peaks (at 776.6 and 787.5 eV, 792.3 and 903.2 eV), respectively (Fig. 2d). However, only one weak Al peak derived from Al^{3+} in the AAH appears at ~75.7 eV (Fig. 2e). In Fig. 2f, the P 2p spectrum can be fitted by three sub-peaks at 129.5, 130.7 and 134.3 eV, which belong to P $2p_{3/2}$, P $2p_{1/2}$ and oxidized phosphate species, respectively [44].

3.2. Exploration of charge separation degree

To explore the influence of the addition of CoP/AAH cocatalyst on the charge separation degree, a series of electrochemical experiments were performed. As shown in Fig. 3a, the photocurrent density of CLP-350 is much higher than that of pristine CdS, which is caused by the greatly promoted charge separation in CLP-350 after introducing the
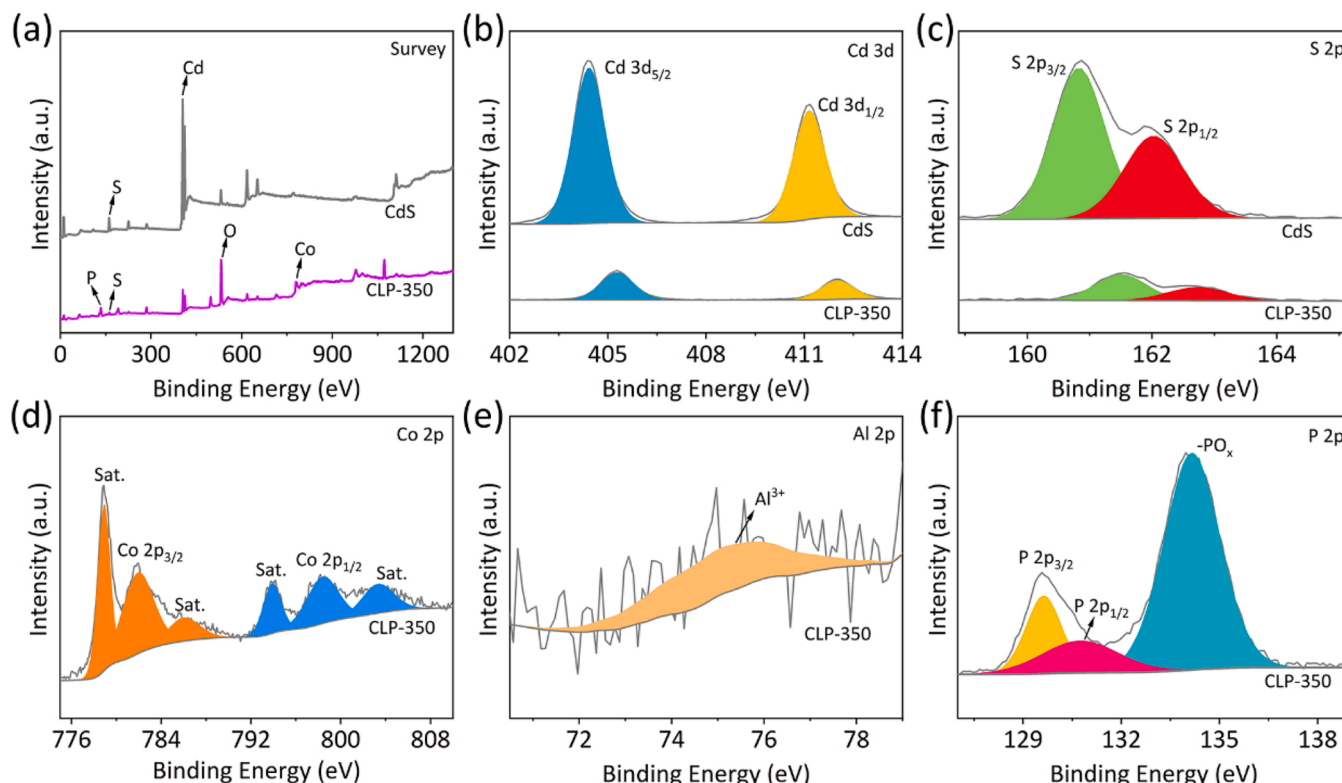

Fig. 2. XPS spectra of (a) survey, (b) Cd 3d, (c) S 2p, (d) Co 2p, (e) Al 2p and (f) P 2p for the pristine CdS and CLP-350 hybrid.
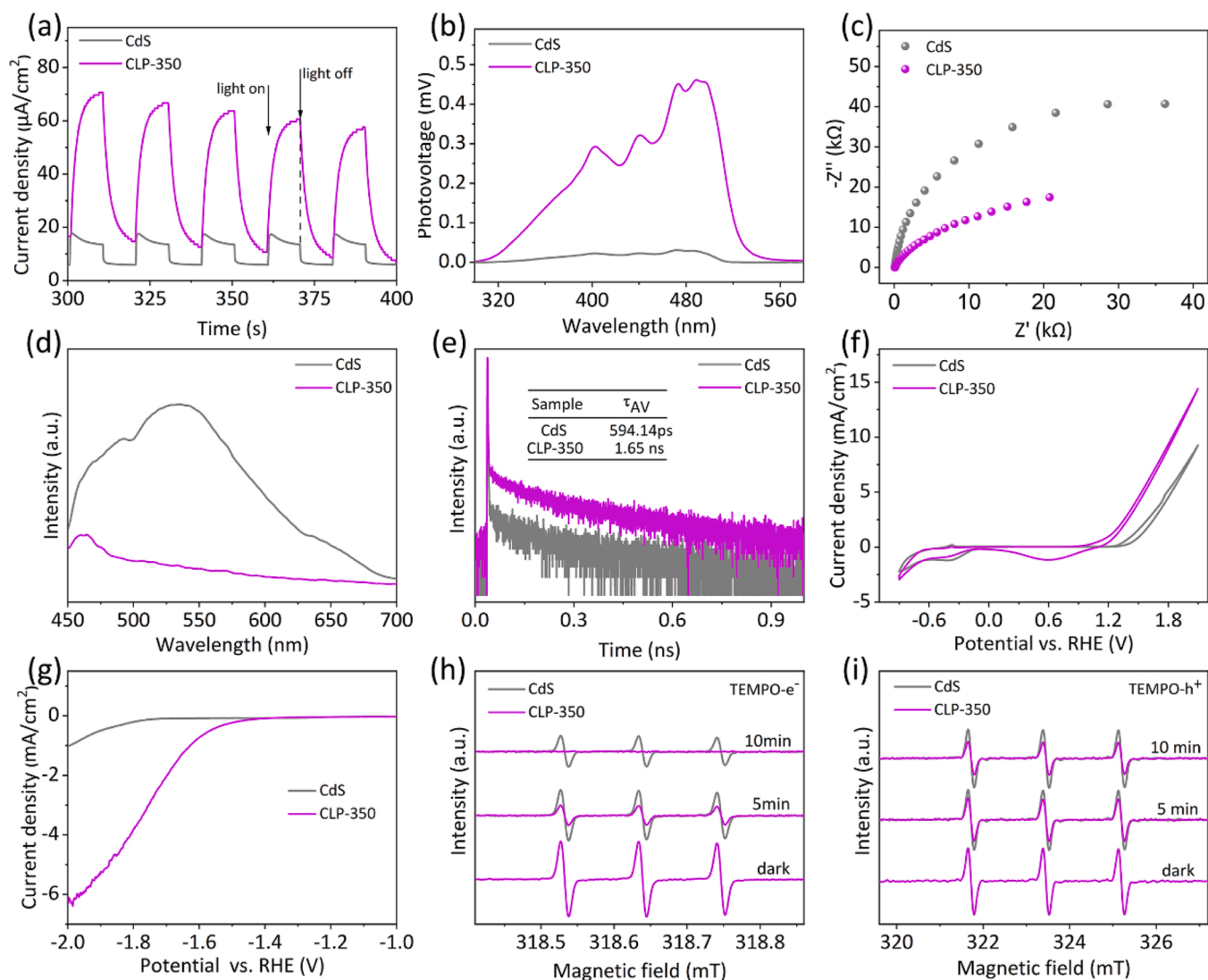
Fig. 3. (a) Photocurrent responses, (b) SPV spectra, (c) EIS plots, (d) PL spectra, (e) TRPL spectra, (f) CV curves, (g) LSV plots, ESR spectra for (h) TEMPO-e$^-$ and (i) TEMPO-h$^+$ of pristine CdS and CLP-350 hybrid.

CoP@AAH. In particular, the slow growth of photocurrent and the long tail occur in the photocurrent curve of CLP-350 when the light is turn on and off, respectively, which should be ascribed to the high density of trap states. The CLP-350 also possesses a higher photovoltage response than the pristine CdS in the wavelength range of 300–560 nm (Fig. 3b), indicating a higher separation efficiency of photogenerated electrons and holes [45–47]. The R_{ct} of CLP-350 is much smaller than that of pristine CdS (Fig. 3c), since the CoP@AAH shell can promote significantly the mobility of charge, thus suppressing the recombination of carriers. Compared with the pristine CdS, the lower PL emission peak intensity of CLP-350 also indicates a higher separation efficiency of photogenerated carriers (Fig. 3d), and the longer lifetime of photogenerated carriers demonstrates a lower recombination rate (Fig. 3e). In the CV plots, the CLP-350 hybrid presents a higher current density than the pristine CdS (Fig. 3f), and the reduction peak of CLP-350 can be ascribed to the Co^{3+}/Co^{2+} redox reaction [48,49]. The photocatalytic HER activity is highly dependent on the overpotential of the HER reaction, so the lower overpotential of CLP-350 suggests a higher photocatalytic H$_2$ production activity (Fig. 3g). Additionally, the CLP-350 hybrid has a higher charge separation rate and a lower HER overpotential than the CdS/Pt according to the electrochemical experimental results of CLP-350 and CdS/Pt (Fig. S6). Furthermore, both the pristine CdS and CLP-350 hybrid present three characteristic peaks of TEMPO-e$^-$

and TEMPO-h$^+$ in dark in the ESR spectra (Fig. 3h and i). When exposed to light, the lower peak intensity reflects that more photo-induced carriers can react with the TEMPO molecules as time goes on. After the irradiation for 5 and 10 min, the CLP-350 hybrid presents lower peak intensity of TEMPO-e$^-$ and TEMPO-h$^+$ than the pristine CdS, indicating much more photo-induced carriers produced in the CLP-350 [50,51]. Therefore, the higher separation efficiency and lower combination rate of photo-generated carriers confirm that the introduction of CoP@AAH can enable the charge to structurally separate. Actually, the photo-generated carriers originated from the CdS surface can transfer out of the shell immediately to participate in the H$_2$ production reaction, instead of accumulating on the CdS surface, thus reducing the photocorrosion.

3.3. Light absorption and band structure

Taking into account that the light utilization is closely related to light absorption of the catalyst, UV–visible diffuse reflectance spectra (UV-Vis DRS) were used to analyze the optical properties of CdS/CoP@AAH hybrids. The absorption edge is located at ~550 nm for pristine CdS, while the absorption edge can hardly be detected for the CdS/CoP@AAH hybrids (Fig. 4a). The absorbance of hybrid climbs at different levels with the CdS concentration decreasing, indicating that the introduction of CoP@AAH can enhance the light absorption. The CLP-350 hybrid
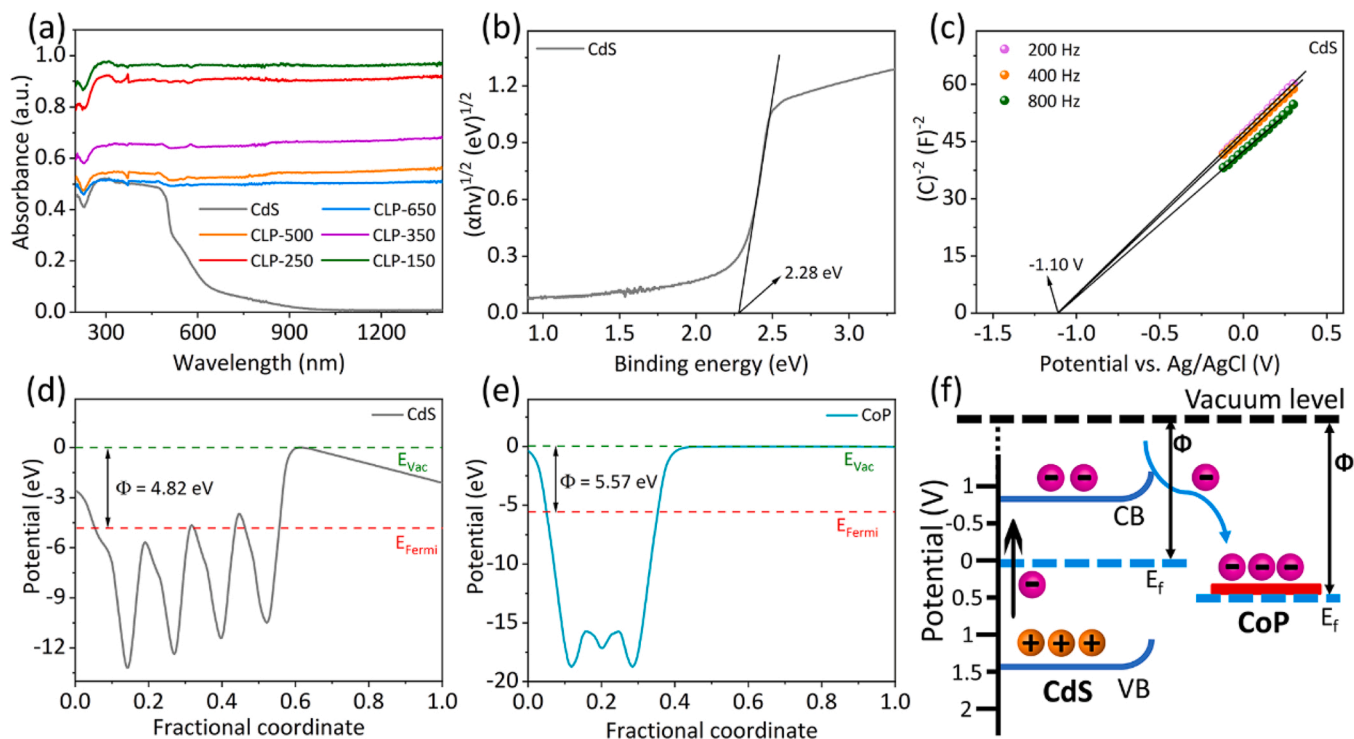
Fig. 4. (a) UV-Vis absorption spectra of CLP hybrids; (b) Kubelka-Munk transformed reflectance spectra and (c) Mott-Schottky plots of pristine CdS; Work functions of (d) pristine CdS and (e) CoP; (f) Band structures and charge transfer of CdS/CoP system.

presents higher absorbance than the pristine CdS, especially in the wavelength range of over 500 nm. Actually, the absorbances of CLP-350 and LDH-P samples are higher than those of CLP-350-ex and LDH-P-ex samples, respectively (Fig. S7), which can also be evidenced by their colors derived from inconsistent products and morphologies (Fig. S8), indicating that the in-situ phosphorization process can contribute to improving the light absorption. The bandgap (Eg) for direct semiconductor can be calculated from the following equation:

$$\alpha h\nu = A(h\nu - E_g)^{1/2} \tag{6}$$

where α, $h\nu$, and A represent the absorption coefficient, photo energy and tail parameter, respectively. The Eg of CdS is calculated to be 2.28 eV (Fig. 4b). The flat band potential (E_{fb}, vs. Ag/AgCl) of CdS is -1.10 V according to the M-S plots (Fig. 4c). The E_{fb} can be converted into the reversible hydrogen electrode potential (E_{RHE}) via the following equation:

$$E_{RHE} = E_{Ag/AgCl} + 0.059 \times pH + E^*_{Ag/AgCl} \tag{7}$$

where the $E^*_{Ag/AgCl}$ and pH of electrolyte are 0.197 V and 6.8, respectively. The conduction band potential (E_{CB}) of n-type semiconductor is usually 0.3 V more negative than the E_{fb}. So, the E_{CB} of CdS can be calculated to be -0.80 V. To clarify the electron flow direction in the hybrid catalyst, the work functions (Φ) of CdS and CoP need to be determined, which are calculated to be 4.82 and 5.57 eV, respectively (Fig. 4d and e). Once the CdS is in contact with the CoP, an equilibrium state between their Fermi levels can be built up, and the electrons of CdS flow to CoP, leading to accumulation of negative charges on the CoP. Meanwhile, the holes are left on CdS. In this diffusion process, the free electrons in the CdS near the CdS/CoP interface are depleted, leaving a space charge region. This makes the energy band of CdS bend upward, thus forming a Schottky barrier (Fig. 4f). When light irradiates the CdS/CoP@AAH hybrid, the photogenerated electrons on the VB of CdS jump to the CB and then flow to the CoP to participate in the H2 evolution reaction, and the Schottky barrier prevents the electrons from flowing back to CdS (Fig. 4f), thus promoting the charge separation.

3.4. Roles of CdS, CoP and AAH in photocatalytic H2 evolution and stability

Fig. 5a—d shows the photocatalytic H2 evolution performance of pristine CdS and CdS/CoP@AAH hybrids in 10 vol% lactic acid and deionized water. The H2 evolution rate firstly climbs and then drops with the CoP@AAH concentration decreasing, arriving at the highest value of 54.9 mmol/g/h for the CLP-350 hybrid, which is ~15 higher than that of pristine CdS (Fig. 5a and b). The high-conductivity CoP plays a pivotal role in this enhancement of photocatalytic activity, since the intimate contact between CoP and CdS can efficiently promote the separation of photogenerated carriers. Meantime, the light absorption is also significantly enhanced. In particular, the CLP-350 hybrid also achieves a H2 evolution rate of 90.6 mmol/g/h under sun light irradiation (Fig. S9c). Moreover, the CdS/Pt hybrid presents a H2 evolution rate of 8.3 mmol/g/h, which is only ~2.3 higher than that of pristine CdS (Fig. S9b). Hence, the CLP-350 hybrid has far higher photocatalytic H2 evolution activity than the CdS/Pt hybrid. The decreasing H2 evolution rates of CLP-500 and CLP-650 can be ascribed to the relatively low concentration of CoP@AAH cocatalyst. Moreover, the H2 evolution rates of CLP-350 samples using different weights of phosphating agent (NaH2PO2·H2O) demonstrate that the 500 mg of NaH2PO2·H2O is adequate to make the LDH completely convert into the CoP/AAH (Fig. S9a), and especially the CLP-350-ex hybrid possess a lower H2 evolution rate than the CLP-350 hybrid (Fig. S9b), which can be ascribed to the insufficient interface contact between the CdS nanorods and CoP (Fig. S3e). In deionized water, the variation trend of the H2 evolution rate is similar to that in 10 vol% lactic acid, and the CLP-350 hybrid also presents the highest photocatalytic H2 evolution rate of 192.1 μmol/g/h (Fig. 5c and d), which can further demonstrate the efficient charge separation caused by CoP@AAH. Furthermore, the H2 evolution rate of pristine CdS drops obviously in the 4th cycle owing to the photocorrosion (Fig. S9d), while the CLP-350 hybrid presents excellent cycle stability due to the complete coverage of CoP@AAH on the CdS nanorods (Fig. 5e). The poor cycle stability is also observed in the CCP-350
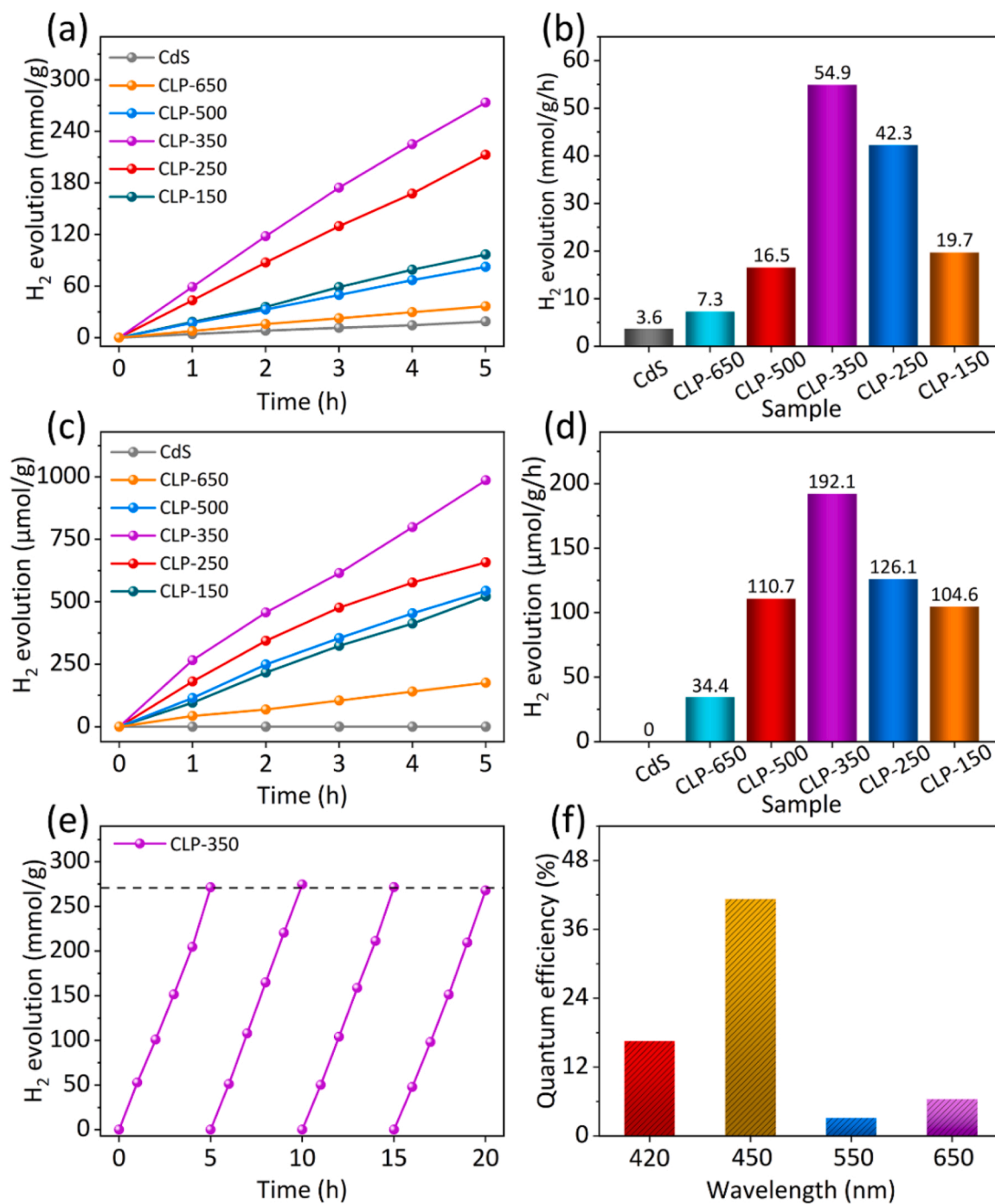
Fig. 5. Photocatalytic H_2 evolution performance of pristine CdS and CdS/CoP@AAH hybrids in (a,b) 10% lactic acid and (c,d) deionized water; (e) Cycle stability for CLP-350 hybrid; (f) Apparent quantum efficiencies of CLP-350 hybrid at different wavelengths of light.

and CAP-350 hybrids in lactic acid (Fig. S9e and f), but a relatively high evolution rate is also obtained in the CCP-350 hybrid, indicating that the only CoP addition can enhance greatly the photocatalytic H_2 evolution performance of CdS, but cannot improve its cycle stability due to the lack of the protection of unique core-shell structure. The weak interface-contact between the large $Al_2(OH)_3F_2$ grains and CdS nanorods in CAP-350 hybrid also cannot benefit the charge separation, resulting in poor photocatalytic H_2 evolution performance and cycle stability.

Moreover, the AQE values of CLP-350 hybrid at 420 and 450 nm arrive at 17.45% and 40.64%, respectively. However, its AQE values at 550 and 650 nm still remain 3%—6% (Fig. 5f and Table S1), which is closely related to the suffered heat treatment of CdS in the

phosphorization process (Fig. S10). Actually, the as-fabricated CLP-350 hybrid possesses not only excellent photocatalytic H_2 production performance (involving H_2 evolution rate and AQE) but also excellent cycle stability compared with other CdS/TMPs composite catalysts under the same illumination of light source in recent years (Table S2), which can be mainly attributed to its unique core-shell structure and the charge transfer mechanism.

To further explore the roles of CoP@AAH on stability of CdS, the XRD patterns, XPS spectra, the concentrations of Cd^{2+} in the sacrificial agent and microstructures of related samples before and/or after 4 cycle experiments were recorded. After photocatalytic HER reaction for 16 h, the diffraction peaks of Cd (JCPDS. 05–0674) emerges in the XRD

pattern of CdS (Fig. 6a). In contrast, no new peak appears in the XRD patterns of CLP-350 before and after the cycle experiments (Fig. 6b), confirming the protection of CoP@AAH shell to CdS. Compared with the CLP-350, a new peak originated from elemental S is produced in the S 2p spectrum of pristine CdS sample after the cycle reaction (Fig. 6c). So, both the XRD and XPS results demonstrate the decomposition of CdS only occurs in the pristine CdS after cycle test. The Cd^{2+} concentrations in the lactic acid for pristine CdS, CCP-350 and CLP-350 samples are measured by ICP-OES (Fig. 6d), indicating that the Cd^{2+} concentration for each sample climbs gradually with the cycle number increasing. The Cd^{2+} concentrations for the CLP-350 samples after 1–4 cycles are all much lower than those for pristine CdS, and meanwhile the Cd^{2+} concentrations for CCP-350 samples are increased in varying degrees compared with those for CLP-350. These results indicate that the CoP@AAH hybrid shell plays a vital role in preventing CdS from decomposing, and only loading of CoP can suppress the photocorrision to some extent due to its high conductivity. Moreover, the surface of pristine CdS nanorods turns from smooth into rough after 4 cycles (Figs. 1b and 6e), while the CdS nanorods in the CLP-350 hybrid remain basically the original state (Figs. 1d and 6f).

Taken all above together, we could draw a conclusion that CoP plays a dominant role in the boosting H_2 evolution rate since the charge separation rate and light absorption is significantly enhanced. Meanwhile, AAH makes a great contribution to the stability of CdS as the unique core/shell structure can prevent the photogenerated hole from accumulating on the CdS surface, thus alleviating photocorrision.

3.5. Interfacial charge behavior and photocatalytic mechanism

To further explore the mechanism behind the enhanced photocatalytic H_2 production, the interfacial charge behavior was analyzed by DFT calculations. The ΔG_{H*} adsorbed on pristine CdS, $CdS/Al_2(OH)_3F_2$ and CdS/CoP are calculated to be 1.10, 1.07 and 0.18 eV, respectively (Fig. 7a). The quite low H* absorption of CdS/CoP demonstrates that the HER reaction can easily occur after the introduction of CoP [52,53], and

the presence of $Al_2(OH)_3F_2$ has no negative effect on the H_2 evolution since the ΔG_{H*} of $CdS/Al_2(OH)_3F_2$ is lower than that of pristine CdS. The charge density distribution between CdS and CoP indicates that the electrons flow from CdS to CoP (Fig. 7b), which is in good agreement with the XPS results (Fig. 2b and c). Moreover, the calculated H_2O adsorbed energies on CdS, CoP and $Al_2(OH)_3F_2$ show the lowest energy of $Al_2(OH)_3F_2$ (−5.16 eV) compared with those of CdS (−0.47 eV) and CoP (−0.17 eV) (Fig. 7c), suggesting that the introduction of AAH shell can promote markedly the dispersion of the catalyst in the sacrificial agent and thus accelerate the HER reaction. This is because the presence of -OH and -F groups in the AAH shell can enhance the hydrophilia of the hybrids, which is in accordance with the corresponding contact angels (Fig. S11). According to the calculated density of state (DOS), the bandgap of CdS is ~1.15 eV (Fig. 7d), indicating a semiconductor characteristic. After absorbing H* , the Fermi energy level (E_f) shifts towards the CB, and meanwhile there is no significant hybridization peaks near E_f (Fig. 7e), indicating that the HER reaction can hardly occur on the CdS surface due to weak interactions between H* and CdS. After decorating by CoP, the bandgap declines to 0.32 eV, accompanying with appearance of many hybridization peaks near the Fermi energy (Fig. 7f), which are mostly caused by the interactions between electrons on p orbital of P and d orbital of Co. Moreover, the projected density of states (PDOSs) reveal the obvious hybridizations among the p orbital of P, s orbital of H and d orbital of Co, which can facilitate the HER reaction (Fig. 7g). In particular, the location of small peak at the position of Fermi energy indicates the significant interactions between H* and CdS/CoP, resulting in the greatly enhanced HER performance.

The schematic mechanisms of the enhanced photocatalytic HER performance and anti-photocorrosion are presented in Fig. 8. For the CdS/CoP hybrid, the electrons on the VB of CdS jump to its CB under light irradiation, and then flow to CoP to combine with the H^+ in the water. The Schottky barrier between CdS and CoP can prevent the photogenerated electrons from going back to CdS, thus promoting the charge separation. However, the HER reaction still occurs near CdS, and the photogenerated carries have the chance to combine with CdS, thus
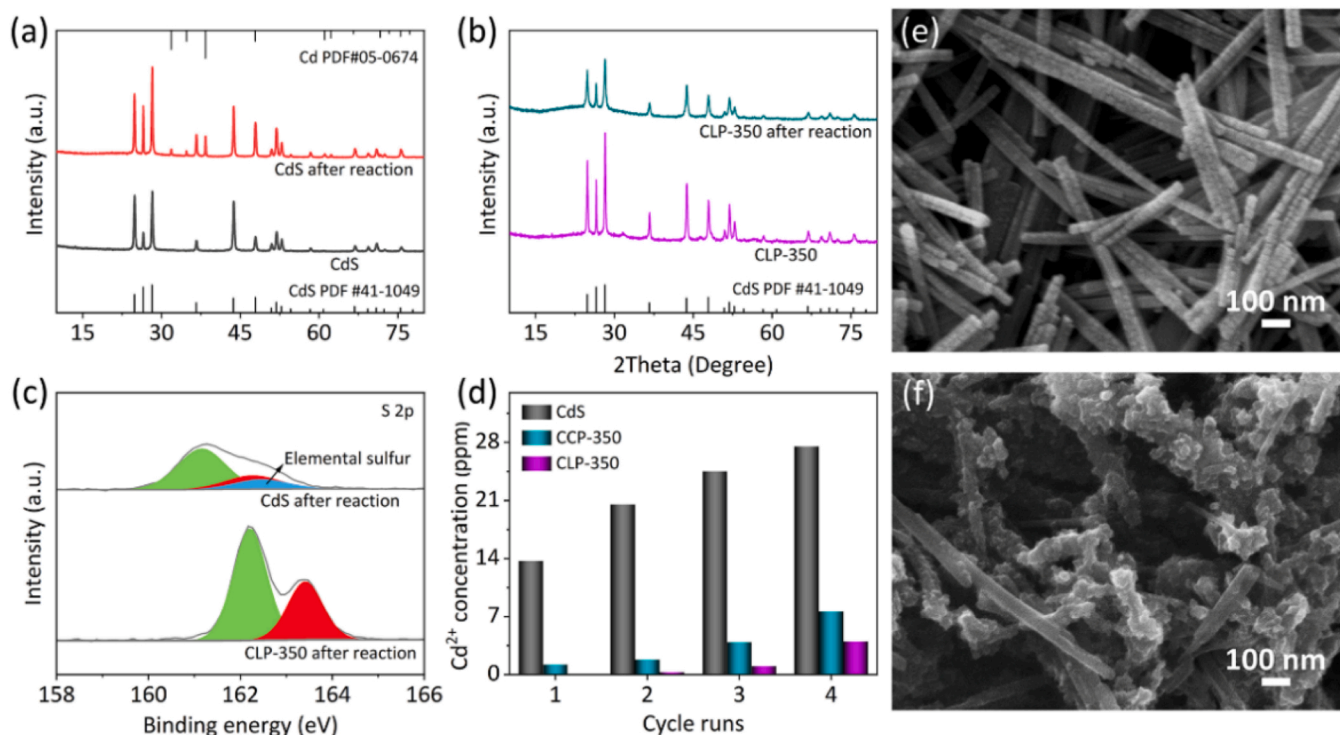

Fig. 6. XRD patterns of (a) pristine CdS and (b) CLP-350 before and after cycle test; (c) XPS spectra of S 2p for pristine CdS and CLP-350 after cycle test; (d) The concentrations of Cd^{2+} in the sacrificial agent for CdS, CCP-350 and CLP-350 after 1–4 cycles; (e,f) SEM images of pristine CdS and CLP-350 after cycle test.
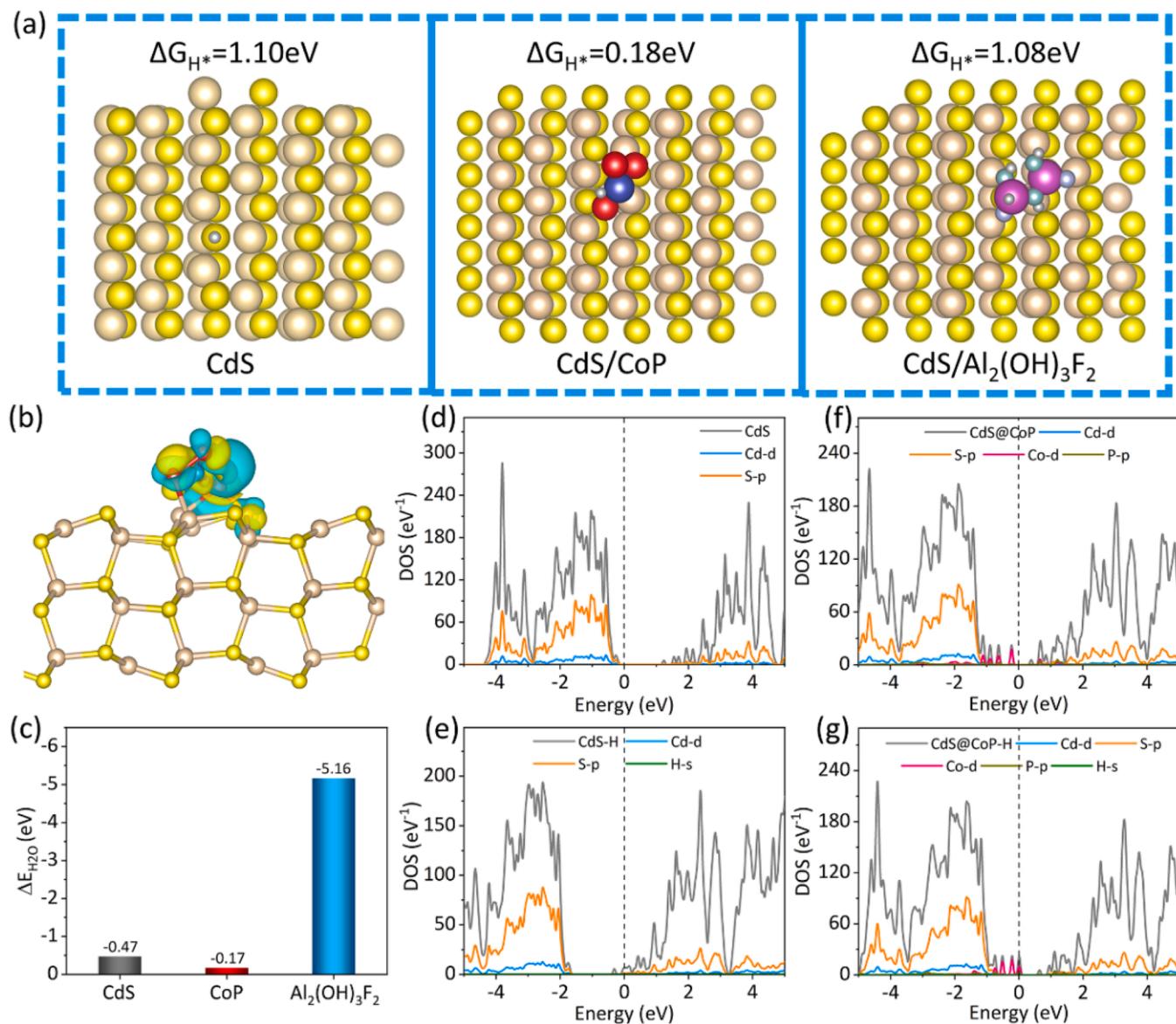
Fig. 7. (a) H* absorbed Gibbs free energies for CdS, CdS/Al$_2$(OH)$_3$F$_2$ and CdS/CoP; (b) Side-view differential charge density map of CdS/CoP; (c) H$_2$O absorbed energies of CdS, CoP and Al$_2$(OH)$_3$F$_2$; DOSs of (d) CdS, (e) CdS-H, (f) CdS/CoP and (g) CdS/CoP-H.
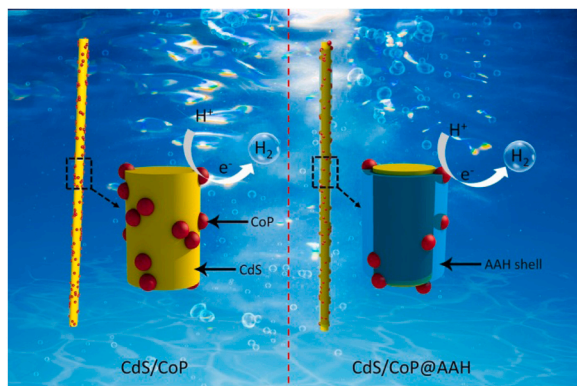

Fig. 8. Photocatalytic H$_2$ production and anti-photocorrosion mechanisms for CdS/CoP@AAH hybrid.

producing the photocorrosion. For the CdS/CoP@AAH hybrid, the AAH shell makes CdS isolate from the sacrificial agent, and the photo-generated carriers migrate out of the shell quickly through the CoP bridge. As a result, the accumulation of charges near CdS is effectively restrained and the photogenerated electrons and holes are separated structurally, thus greatly improving the anti-photocorrosion and pho-tocatalytic H$_2$ evolution of CdS.

4. Conclusion

A novel CoP@AAH cocatalyst was firstly designed and fabricated to hybridize with CdS nanorods via the in-situ phosphorization process. The microstructural analysis confirms that the AAH covers completely the CdS nanorods and the CoP nanoparticles are embedded in the AAH coating, forming a unique core/shell structure. The photo-electrochemical measures demonstrate that the introduction of CoP@AAH can significantly promote the charge separation. The unique core/shell structure contributes to improving the anti-photocorrosion and photocatalytic activity of CdS, where the AAH shell makes CdS isolate from the sacrificial agent, and the CoP acts as a bridge for fast

migration of the photogenerated carriers out of the shell. The optimized CdS/CoP@AAH hybrid presents a photocatalytic H_2 evolution rate of 54.9 mmol/g/h, apparent quantum efficiency (AQE) of 40.62% and excellent cycle stability. DFT calculations further confirm the formation of Schottky heterojunction, significant interactions between CdS and CoP, and the lower ΔG_{H*} of CdS/CoP heterojunction. This work offers a new strategy for enhancing the stability and photocatalytic H_2 evolution of CdS-based catalysts by structurally separating the photogenerated carries.

CRediT authorship contribution statement

Junnan Tao: Conceptualization, Methodology, Investigation, Writing – original draft. **Mingyuan Wang:** Formal analysis, Software, Writing – original draft. **Xiangzhao Zhang**: Resource, Software. **Lei Lu:** Funding acquisition. **Hua Tang:** Methodology, Supervision, Funding acquisition. **Qinqin Liu:** Methodology. **Shuangying Lei:** Software. **Guanjun Qiao:** Resource, Funding acquisition. **Guiwu Liu:** Formal analysis, Investigation, Supervision, Funding acquisition, Writing – review & editing.

Declaration of Competing Interest

The authors declare that they have no known competing financial interests or personal relationships that could have appeared to influence the work reported in this paper.

Data Availability

No data was used for the research described in the article.

Acknowledgments

Appendix A. Supporting information

Supplementary data associated with this article can be found in the online version at doi:10.1016/j.apcatb.2022.122004.

References

[1] Q. Wang, J. Warnan, S. Rodríguez-Jiménez, J.J. Leung, S. Kalathil, V. Andrei, K. Domen, E. Reisner, Molecularly engineered photocatalyst sheet for scalable solar formate production from carbon dioxide and water, Nat. Energy 5 (2020) 703–710.

[2] H. Luo, J. Barrio, N. Sunny, A. Li, L. Steier, N. Shah, I.E.L. Stephens, M.M. Titirici, Progress and perspectives in photo- and electrochemical-oxidation of biomass for sustainable chemicals and hydrogen production, Adv. Energy Mater. 11 (2021), 2101180.

[3] B. You, G.Q. Han, Y.J. Sun, Electrocatalytic and photocatalytic hydrogen evolution integrated with organic oxidation, Chem. Commun. 54 (2018) 5943–5955.

[4] A. Fujishima, K. Honda, Electrochemical photolysis of water at a semiconductor electrode, Nature 238 (1972) 37–38.

[5] Z.P. Li, W.X. Huang, J.X. Liu, K.L. Lv, Q. Li, Embedding CdS@Au into ultrathin $Ti_{3-x}C_2T_y$ to build dual schottky barriers for photocatalytic H_2 production, ACS Catal. 11 (2021) 8510–8520.

[6] Y. Hu, X.H. Yu, Q.Q. Liu, L.L. Wang, H. Tang, Highly metallic Co-doped MoS_2 nanosheets as an efficient cocatalyst to boost photoredox dual reaction for H_2 production and benzyl alcohol oxidation, Carbon 188 (2022) 70–80.

[7] H.C. Yang, R.Y. Cao, P.X. Sun, J.M. Yin, S.W. Zhang, X.J. Xu, Constructing electrostatic self-assembled 2D/2D ultra-thin $ZnIn_2S_4$/protonated g-C_3N_4 heterojunctions for excellent photocatalytic performance under visible light, Appl. Catal. B Environ. 256 (2019), 117862.

[8] P. Zhou, Q.H. Zhang, Z.K. Xu, Q.Y. Shang, L. Wang, Y.G. Chao, Y.J. Li, H. Chen, F. Lv, Q. Zhang, L. Gu, S.J. Guo, Atomically dispersed Co–P_3 on CdS nanorods with electron-rich feature boosts photocatalysis, Adv. Mater. 32 (2020), 1904249.

[9] Z. Fiqar, J.N. Tao, T. Yang, Q.Q. Liu, J. Hu, H. Tang, Designing 0D/2D CdS nanoparticles/g-C_3N_4 nanosheets heterojunction as efficient photocatalyst for improved H_2-evolution, Surf. Interfaces 26 (2021), 101312.

[10] D.T. You, C.X. Xu, X.X. Wang, J. Wang, W.Y. Su, R. Wang, T.L. Chen, R. Wang, Z. L. Shi, A core@dual-shell nanorod array with a cascading band configuration for enhanced photocatalytic properties and anti-photocorrosion, J. Mater. Chem. A 8 (2020) 3726–3734.

[11] J.R. Huang, J.N. Tao, G.W. Liu, L. Lu, H. Tang, G.J. Qiao, In situ construction of 1D CdS/2D Nb_2CT_x MXene Schottky heterojunction for enhanced photocatalytic hydrogen production activity, Appl. Surf. Sci. 573 (2022), 151491.

[12] T.Y. Zhu, Y.J. Liang, Y.N. Wang, J. Wang, W.Z. Wang, J.L. Fu, L.Z. Yao, Y. Cheng, H.S. Han, P-type β-Ni(OH)₂ nanoparticles sensitize CdS nanorod array photoanode to prolong charge carrier lifetime and highly improve bias-free visible-light-driven H_2 evaluation, Appl. Catal. B Environ. 271 (2020), 118945.

[13] L. Cheng, Q.J. Xiang, Y.L. Liao, H.W. Zhang, CdS-based photocatalysts, Energy Environ. Sci. 11 (2018) 1362–1391.

[14] K.H. Yang, Z.Z. Yang, C. Zhang, Y.L. Gu, J.J. Wei, Z.H. Li, C. Ma, X. Yang, K. X. Song, Y.M. Li, Q.Z. Fang, J.W. Zhou, Recent advances in CdS-based photocatalysts for CO_2 photocatalytic conversion, Chem. Eng. J. 418 (2021) 129344.

[15] R.C. Shen, D.D. Ren, Y.N. Ding, Y.T. Guan, Y.H. Ng, P. Zhang, X. Li, Nanostructured CdS for efficient photocatalytic H_2 evolution: A review, Sci. China Mater. 63 (2020) 2153–2188.

[16] J.A. Nasir, Z.U. Rehman, S.N.A. Shah, A. Khan, I.S. Butler, C.R.A. Catlow, Recent developments and perspectives in CdS-based photocatalysts for water splitting, J. Mater. Chem. A 8 (2020) 20752–20780.

[17] G.Q. Liu, Y. Li, Y. Yang, F.J. Fan, G.H. Ding, L. Wu, J. Hu, J.L. Peng, Q. Xu, J.F. Zhu, S.H. Yu, Anti-photocorrosive photoanode with RGO/PdS as hole extraction layer, Sci. China Mater. 63 (2020) 1939–1947.

[18] Z.Y. Lu, G.S. Zhou, M.S. Song, X.L. Liu, H. Tang, H.J. Dong, P.W. Huo, F. Yan, P. Du, G.Z. Xing, Development of magnetic imprinted PEDOT/CdS heterojunction photocatalytic nanoreactors: 3-Dimensional specific recognition for selectively photocatalyzing danofloxacin mesylate, Appl. Catal. B Environ. 268 (2020), 118433.

[19] H. Li, X.Q. Yan, B. Lin, M.Y. Xia, J.J. Wei, B.L. Yang, G.D. Yang, Controllable spatial effect acting on photo-induced CdS@CoP@SiO₂ ball-in-ball nano-photoreactor for enhancing hydrogen evolution, Nano Energy 47 (2018) 481–493.

[20] J.N. Tao, M.Y. Wang, G.W. Liu, Q.Q. Liu, L. Lu, N. Wan, H. Tang, G.J. Qiao, Efficient photocatalytic hydrogen evolution coupled with benzaldehyde production over 0D $Cd_{0.5}Zn_{0.5}S$/2D Ti_3C_2 Schottky heterojunction, J. Adv. Ceram. 11 (2022) 1117–1130.

[21] X.F. Ning, G.X. Lu, Photocorrosion inhibition of CdS-based catalysts for photocatalytic overall water splitting, Nanoscale 12 (2020) 1213–1223.

[22] R. Xiao, C.X. Zhao, Z.Y. Zou, Z.P. Chen, L. Tian, H.T. Xu, H. Tang, Q.Q. Liu, Z. X. Lin, X.F. Yang, In situ fabrication of 1D CdS nanorod/2D Ti_3C_2 MXene nanosheet Schottky heterojunction toward enhanced photocatalytic hydrogen evolution, Appl. Catal. B Environ. 268 (2020), 118382.

[23] S.C. Cai, M. Zhang, J.J. Li, J. Chen, H.P. Jia, Anchoring single-atom Ru on CdS with enhanced CO_2 capture and charge accumulation for high selectivity of photothermocatalytic CO_2 reduction to solar fuels, Sol. RRL 5 (2021), 2000313.

[24] Z.Y. Mo, W.Y. Yang, S. Gao, J.K. Shang, Y.J. Ding, W.Z. Sun, Q. Li, Efficient oxygen reduction reaction by a highly porous, nitrogen-doped carbon sphere electrocatalyst through space confinement effect in nanopores, J. Adv. Ceram. 10 (2021) 714–728.

[25] J. Wu, L.Y. Li, X.A. Li, X. Min, Y. Xing, A novel 2D graphene oxide modified α-$AgVO_3$ nanorods: design, fabrication, and enhanced visible-light photocatalytic performance, J. Adv. Ceram. 11 (2022) 308–320.

[26] L.Z. Wang, R. Tang, A. Kheradmand, Y.J. Jiang, H. Wang, W.J. Yang, Z.B. Chen, X. Zhong, S.P. Ringer, X.Z. Liao, W.B. Liang, J. Huang, Enhanced solar-driven benzaldehyde oxidation with simultaneous hydrogen production on Pt single-atom catalyst, Appl. Catal. B Environ. 284 (2021) 119759.

[27] W. Chen, B.B. Wu, Y.Y. Wang, W. Zhou, Y.Y. Li, T.Y. Liu, C. Xie, L.T. Xu, S.Q. Du, M.L. Song, D.D. Wang, Y.B. liu, Y.F. Li, J.L. Liu, Y.Q. Zou, R. Chen, C. Chen, J. Y. Zheng, Y.F. Li, J. Chen, S.Y. Wang, Deciphering the alternating synergy between interlayer Pt single-atom and NiFe layered double hydroxide for overall water splitting, Energy Environ. Sci. 14 (2021) 6428–6440.

[28] Y.W. Liu, W.X. Yang, Q.L. Chen, D.A. Cullen, Z.X. Xie, T.Q. Lian, Pt particle size affects both the charge separation and water reduction efficiencies of CdS–Pt nanorod photocatalysts for light driven H_2 generation, J. Am. Chem. Soc. 144 (2022) 2705–2715.

[29] D.D. Ren, Z.Z. Liang, Y.H. Ng, P. Zhang, Q.J. Xiang, X. Li, Strongly coupled 2D–2D nanojunctions between P-doped Ni_2S (Ni_2SP) cocatalysts and CdS nanosheets for efficient photocatalytic H_2 evolution, Chem. Eng. J. 390 (2020), 124496.

[30] W.L. Zhen, X.F. Ning, B.J. Yang, Y.Q. Wu, Z. Li, G.X. Lu, The enhancement of CdS photocatalytic activity for water splitting via anti-photocorrosion by coating Ni_2P shell and removing nascent formed oxygen with artificial gill, Appl. Catal. B Environ. 221 (2018) 243–257.

[31] X.Q. Xie, N. Zhang, Z.R. Tang, M. Anpo, Y.J. Xu, $Ti_3C_2T_x$ MXene as a Janus cocatalyst for concurrent promoted photoactivity and inhibited photocorrosion, Appl. Catal. B Environ. 237 (2018) 43–49.

[32] X. Liu, Y.X. Zhao, X.F. Yang, Q.Q. Liu, X.H. Yu, Y.Y. Li, H. Tang, T.R. Zhang, Porous Ni_5P_4 as a promising cocatalyst for boosting the photocatalytic hydrogen evolution reaction performance, Appl. Catal. B Environ. 275 (2020) 119144.

[33] L.P. Zhang, J.T. Zhang, J.J. Fang, X.Y. Wang, L.K. Yin, W. Zhu, Z.B. Zhuang, Cr-doped CoP nanorod arrays as high-performance hydrogen evolution reaction catalysts at high current density, Small 17 (2021), 2100832.

[34] Y.L. Meng, J. Tang, X. Chen, Z.Y. Niu, Y.H. Zhao, Y. Pan, X.F. Wang, X.Z. Song, Z. Tan, Hierarchical particle-on-sheet CoP fabricated by direct phosphorization of Co(OH)$_2$/ZIF-67 hybrid for boosting hydrogen evolution electrocatalysis, Inorg. Chem. Commun. 134 (2021) 109058.

[35] F.F. Shang, S.H. Wan, X.Q. Gao, W. Zhang, R. Cao, Engineering hierarchical-dimensional Co(OH)F into CoP superstructure for electrocatalytic water splitting, ChemCatChem 12 (2020) 4770–4774.

[36] J.N. Tao, X.H. Yu, Q.Q. Liu, G.W. Liu, H. Tang, Internal electric field induced S–scheme heterojunction MoS$_2$/CoAl LDH for enhanced photocatalytic hydrogen evolution, J. Colloid Interface Sci. 585 (2021) 470–479.

[37] T.Y. Wang, Y. Yang, Q.H. Deng, X.Y. Zhang, L.J. Xiong, Z. Tang, P.J. Li, N. Yin, A. W. Sun, D. Chen, J.Y. Shen, In-situ construction of 3D marigold-like CoAl-LDH/Ti$_3$C$_2$ heterosystem collaborating with 2D/2D interface for efficient photodegradation of multiple antibiotics, Appl. Surf. Sci. 569 (2021) 151084.

[38] P.F. Yue, H.D. She, L. Zhang, B. Niu, R. Lian, J.W. Huang, L. Wang, Q.Z. Wang, Super-hydrophilic CoAl-LDH on BiVO$_4$ for enhanced photoelectrochemical water oxidation activity, Appl. Catal. B Environ. 286 (2021), 119875.

[39] J.P. Perdew, K. Burke, M. Ernzerhof, Generalized gradient approximation made simple, Phys. Rev. Lett. 77 (1996) 3865–3868.

[40] M.Y. Wang, R.F. Song, Q. Zhang, C.Y. Li, Z.W. Xu, G.W. Liu, N. Wan, S.Y. Lei, Synergy effect of Cu-Ru dual atoms anchored to N-doped phosphorene for nitrogen reduction reaction, Fuel 321 (2022), 124101.

[41] Y. Liu, J.X. Sun, X. Zhou, C.D. Lv, Y.S. Zhou, B.W. Cong, G. Chen, An in-plane S-scheme heterostructure drives H$_2$ production with water and solar energy, Chem. Eng. J. 437 (2022), 135280.

[42] Z.L. Jin, L.J. Zhang, G.R. Wang, Y.B. Li, Y.B. Wang, Graphdiyne formed a novel CuI-GD/g-C$_3$N$_4$ S-scheme heterojunction composite for efficient photocatalytic hydrogen evolution, Sustain. Energy Fuels 4 (2020) 5088–5101.

[43] X.B. Li, B.B. Kang, F. Dong, Z.Q. Zhang, X.D. Luo, L. Han, J.T. Huang, Z.J. Feng, Z. Chen, J.L. Xu, B.L. Peng, Z.L. Wang, Enhanced photocatalytic degradation and H$_2$/H$_2$O$_2$ production performance of S-pCN/WO$_{2.72}$ S-scheme heterojunction with appropriate surface oxygen vacancies, Nano Energy 81 (2021) 105671.

[44] Y. Zhao, Y.F. Lu, L. Chen, X.F. Wei, J.F. Zhu, Y.H. Zheng, Redox dual-cocatalyst-modified CdS double-heterojunction photocatalysts for efficient hydrogen production, ACS Appl. Mater. Interfaces 12 (2020) 46073–46083.

[45] Y. Lin, Q. Zhang, Y.H. Li, Y.P. Liu, K.J. Xu, J.N. Huang, X.S. Zhou, F. Peng, The evolution from a typical type-I CdS/ZnS to type-II and Z-scheme hybrid structure for efficient and stable hydrogen production under visible light, ACS Sustain. Chem. Eng. 8 (2020) 4537–4546.

[46] J.F. Gao, F.D. Zhang, H.Q. Xue, L.H. Zhang, Y. Peng, X.L. Li, Y.Q. Gao, N. Li, G. Lei, In-situ synthesis of novel ternary CdS/PdAg/g-C$_3$N$_4$ hybrid photocatalyst with significantly enhanced hydrogen production activity and catalytic mechanism exploration, Appl. Catal. B Environ. 281 (2021) 119509.

[47] Y.Y. Li, Q.N. Wu, Q.J. Bu, K. Zhang, Y.H. Lin, D.J. Wang, X.X. Zou, T.F. Xie, An effective CdS/Ti-Fe$_2$O$_3$ heterojunction photoanode: Analyzing Z-scheme charge-transfer mechanism for enhanced photoelectrochemical water-oxidation activity, Chin. J. Catal. 42 (2021) 762–771.

[48] X.X. Zhang, G.M. Qu, Z.H. Wang, G.T. Xiang, S.H. Hao, X.K. Wang, X.J. Xu, W. X. Ma, G. Zhao, Hollow polyhedron structure of amorphous Ni-Co-S/Co(OH)$_2$ for high performance supercapacitors, Chin. Chem. Lett. 32 (2021) 2453–2458.

[49] T.K. Wang, S.S. Zhao, G.M. Qu, J.C. Leng, X.J. Xu, An electrochemical activation strategy boosted alkaline Zinc-ion battery with ultra-high energy density, J. Colloid Interface Sci. 615 (2022) 293–301.

[50] P. Wang, X.B. Zhou, Y. Shao, D.Z. Li, Z.F. Zuo, X.Z. Liu, CdS quantum dots-decorated InOOH: Facile synthesis and excellent photocatalytic activity under visible light, J. Colloid Interface Sci. 601 (2021) 186–195.

[51] C. Ding, C.X. Zhao, S. Cheng, X.F. Yang, Ultrahigh photocatalytic hydrogen evolution performance of coupled 1D CdS/1T-phase dominated 2D WS$_2$ nanoheterojunctions, Chin. J. Catal. 43 (2022) 403–409.

[52] P. Zhou, Q.H. Zhang, Y.G. Chao, L. Wang, Y.J. Li, H. Chen, L. Gu, S.J. Guo, Partially reduced Pd single atoms on CdS nanorods enable photocatalytic reforming of ethanol into high value-added multicarbon compound, Chem 7 (2021) 1033–1049.

[53] M.Y. Zhang, S.Y. Nie, T. Cheng, Y. Feng, C.C. Zhang, L. Zheng, L. Wu, W.C. Hao, Y. Ding, Enhancing the macroscopic polarization of CdS for piezo-photocatalytic water splitting, Nano Energy 90 (2021), 106635.